Water Cladded Plasmonic Slot Waveguide Vertically Coupled With Si$_3$N$_4$ Photonics

George Dabos
Dimitra Ketzaki
Athanasios Manolis
Evaggelia Chatzianagnostou
Laurent Markey
Jean-Claude Weeber
Alain Dereux
Anna Lena Giesecke
Caroline Porschatis
Bartos Chmielak
Dimitris Tsiokos
Nikos Pleros
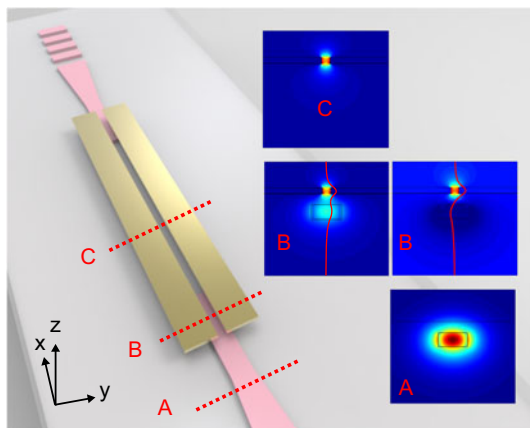
Water Cladded Plasmonic Slot Waveguide Vertically Coupled With Si₃N₄ Photonics

George Dabos [ORCID],[1] **Dimitra Ketzaki,**[1] **Athanasios Manolis,**[1]
Evaggelia Chatzianagnostou [ORCID],[1] **Laurent Markey,**[2]
Jean-Claude Weeber,[2] **Alain Dereux,**[2] **Anna Lena Giesecke,**[3]
Caroline Porschatis,[3] **Bartos Chmielak,**[3] **Dimitris Tsiokos,**[1]
and Nikos Pleros [ORCID] [1]

[1]Department of Informatics, Center for Interdisciplinary Research and Innovation, Aristotle
University of Thessaloniki, Thessaloniki 57001, Greece
[2]Laboratoire Interdisciplinaire Carnot de Bourgogne, UMR 6303 CNRS, Université
Bourgogne Franche Comté, Dijon 21078, France
[3]AMO GmbH, Advanced Microelectronic Center Aachen, Aachen 52074, Germany

Abstract: We demonstrate a water cladded plasmo-photonic waveguide, by exploiting the directional coupling scheme to vertically divert light from a 360×800 nm (height $\times$ width) Si₃N₄ waveguide to a plasmonic slot waveguide, enabling the excitation of a pure plasmonic mode within a 210-nm-wide slot at 1550 nm. The 150-nm-thick plasmonic slot waveguide was deposited on the top of an oxide cladded Si₃N₄ waveguide exhibiting an experimental plasmonic-to-photonic insertion loss of 2.24 ± 0.3 dB and a plasmonic propagation length (L_{spp}) of 10.8 μm at 1550 nm. The proposed plasmo-photonic waveguide holds a promise as an optical transducer element for highly sensitive and low-cost interferometric biosensors due to the significant phase change achieved per unit propagation length.

Index Terms: Photonic integrated circuits, plasmonics, surface plasmons, directional coupling, plasmonic waveguide, silicon nitride, vertical integration.

1. Introduction

Co-integration of plasmonics with silicon photonics emerges as a key-enabling technology towards powerful photonic-integrated-circuits (PICs) combining the benefits of both technologies [1]–[7]. The unique feature of plasmonic waveguides to guide Surface-Plasmon-Polariton (SPP) modes at dimensions beyond the diffraction limit allows for increased light-matter interaction at the nanoscale, hence facilitating miniaturization of photonic devices. However, in most cases plasmonic waveguides exhibit high propagation losses preventing their broad deployment. To overcome this barrier, selective co-integration of plasmonic waveguides in restricted areas of low-loss silicon photonic chips, can mitigate the excessive optical loss coming from plasmonic structures while fully exploiting their functional benefits. An indicative application example where plasmonic waveguides may surpass the performance of photonic waveguides is optical biosensing. In such scenario, the predominant exposure of light at the metal surface offers unmatched refractive index sensing capabilities in micrometer scale propagation distances [8]. In this direction, open-cladded plasmonic

waveguides with strong field dependence on liquid loadings need to be integrated with low loss photonics in compact dimensions and by using simple fabrication methods.

Various in-plane plasmonic waveguides have been co-integrated so far with silicon [8]–[28] or silica-on-silicon photonics [29], targeting either mature classical or promising quantum sensing systems [30], [31]. Specifically, Metal-Insulator-Metal (MIM) or plasmonic slot-based waveguides have attracted significant research interest due to their ability to support deep sub-wavelength confined SPP modes as opposed to stripe based SPP waveguides with decreased mode confinement [29]. However, only a few approaches to demonstrate open cladded plasmonic slot waveguides topped with water have been so far investigated, employing silicon-based photonic waveguides to excite the SPP mode. A hybrid plasmonic mode was excited in a double slot configuration using waveguide tapering in [8] while vertical directional coupling combined with Fabry-Perot resonance was exploited in [9]. In both approaches the potential of hybrid plasmonic slot waveguides in integrated biosensors has been demonstrated further supporting the trend of plasmo-photonic integration. However, in the vertical coupling approach, the existence of the photonic waveguide below the plasmonic slot, forces the hybrid mode to oscillate between the photonic waveguide and the plasmonic slot throughout the complete cavity structure reducing the overall mode interaction with the cladding analyte. In fact, the transition of the mode from the photonic waveguide to the plasmonic slot for pure SPP propagation in the slot region requires the interruption of the photonic waveguide soon after the optical coupling length is met. To address the above requirement, in this work, we rely on our preliminary numerical design that was reported in [23] to demonstrate experimentally, a 150 nm thick gold (Au) based plasmonic slot waveguide cladded with water with a slot width of 210 nm being vertical directionally coupled with low-loss interrupted waveguides with cross-sectional dimensions of 360×800 nm (height $\times$ width). A Si_3N_4 strip lying below a 660 nm thick oxide cladding (H_{clad} 300 nm) was interrupted after a certain overlapping length with the plasmonic slot, allowing for the full utilization of the pure plasmonic SPP mode exposed on top of the structure in sensing applications. Experimental measurements in agreement with numerical simulations, revealed a photonic-to-plasmonic interface insertion-loss (I.L.) of 2.24 ± 0.3 dB and a plasmonic propagation loss of 0.4 dB at 1550 nm, which translates to a plasmonic propagation length (defined as the power decay at 1/e) off 10.8 μm in aqueous environment. The proposed plasmo-photonic waveguide requires a rather simplified and low-cost fabrication process by allowing the plasmonic slot to be deposited directly above the waveguide cladding avoiding any additional etching steps. In addition, compared to butt-coupled approaches, our directional coupling approach resulted in comparable insertion loss values [24]–[26], avoiding more challenging fabrication processes aiming at tapered structures with narrow taper-tips.

The rest of the paper is organized as follows. In Section 2, we present the optimized design and numerical simulations for the vertical photonic-to-plasmonic interface using a commercial available simulation software [32], [33]. Section 3, describes the fabrication process that was followed and the obtained experimental results after conducting broadband optical measurements using grating-couplers (GCs). In Section 4, we assess theoretically the sensitivity of the proposed waveguide in refractive index changes of the liquid cladding in an attempt to evaluate its potential in plasmo-photonic biosensor.

2. Design and Simulation

Fig. 1(a) illustrates a conceptual schematic of the proposed plasmo-photonic waveguide. The plasmonic slot waveguide is deposited on top of an oxide cladded Si_3N_4 waveguide that is interrupted after a certain overlapping length with the plasmonic waveguide. When the photonic and the plasmonic waveguides overlap, a hybrid plasmonic slot waveguide is formed supporting two hybridized plasmonic-photonic modes with even and odd symmetries. In this state, a beating between those modes occurs allowing power exchange between the photonic and the plasmonic waveguides. The maximum power transfer that can be achieved between the photonic and the pure plasmonic SPP mode is predominantly determined by this overlapping length, named as coupling length (L_c) following the principles of directional coupling mechanism [34].
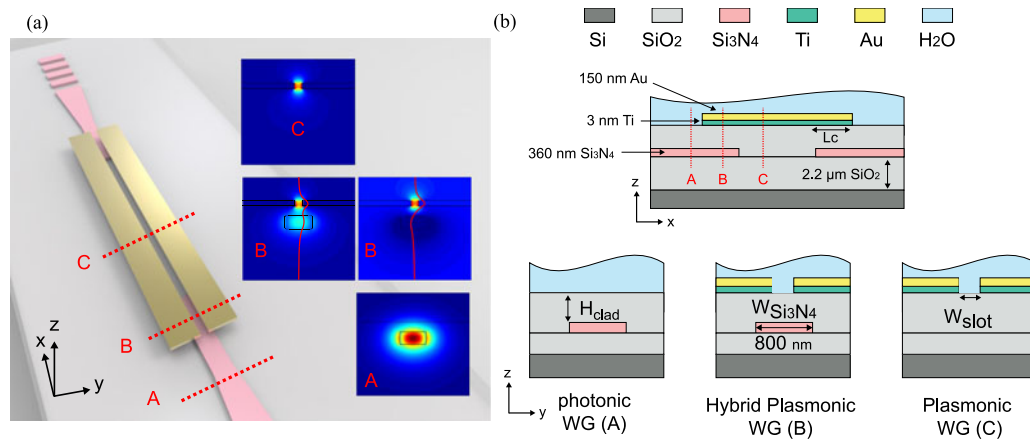
Fig. 1. (a) Conceptual schematic illustrating the vertically coupled plasmonic slot waveguide with Si_3N_4 photonics and the evolution of a photonic mode along the direction of propagation until it is converted to the pure SPP mode. The gold based plasmonic slot waveguide is deposited on top of the oxide cladding of the Si_3N_4 waveguide. Water is not shown for clarity. (b) Side-view and cross sections of the proposed plasmo-photonic waveguide across the different stages of the structure.

A side-view representation of the investigated structure cladded with water, and the cross-sectional dimensions of the employed waveguides along the direction of propagation are shown in Fig. 1(b). More specifically, in our designs we considered a 150 nm thick Au based plasmonic slot waveguide lying on top of a 3 nm thick Ti layer which was used as an adhesion layer between the gold and the oxide cladding of the Si_3N_4 waveguide. For the photonic waveguides, we employed a commercial available Si_3N_4 waveguide platform developed by AMO GmbH, with 360×800 nm strip based waveguides cladded with SiO_2 (Low-Temperature-Oxide- LTO) lying on top of a 2.2 μm thick SiO_2. The design parameters that we investigated based on our fabrication readiness was the height of the cladding in-between the Si_3N_4 top surface and the bottom of the plasmonic waveguide (H_{clad}) as well as the width of the plasmonic slot (W_{slot}) waveguide.

In a first step, we conducted numerical simulations to calculate the effective refractive index (n_{eff}) and the plasmonic propagation length (defined as the power decay at $1/e - L_{spp}$) of the pure SPP mode for slot widths starting from 100 to 250 nm, using the commercial-grade simulator eigenmode solver of *Lumerical Solutions* software. We opted for a W_{slot} of 200 nm targeting at increased L_{spp} lengths and a plasmonic n_{eff} around 1.55 being close that of the photonic mode being 1.57 at 1550 nm. Fig. 2(a) presents the n_{eff} values as wells as the L_{spp} lengths for the SPP mode. Secondly, we investigated more in detail the dependence of the n_{eff} of the hybrid modes that exhibit even and odd symmetries for various cladding thicknesses H_{clad} as presented in Fig. 2(b). The coupling length L_c required to achieve maximum energy transfer between the photonic and the pure SPP modes was estimated using the following relationship $L_c = \frac{\pi}{\beta_{even} - \beta_{odd}}$, where β is the propagation constant at 1550 nm. Next we performed full 3 D Finite-Difference-Time-Domain (FDTD) simulations to evaluate the I.L. of the plasmonic-to-photonic interface using the approximate L_c obtained for H_{clad} values of 200, 250, 300 and 350 nm. Fig. 2(c) presents the simulated I.L. for different L_c values suggesting a minimum I.L. of 1.35 dB at 1550 nm for H_{clad} of 300 nm. One would expect that the minimum I.L. would occur for the shortest L_c, therefore smaller H_{clad} values, however it was observed that a local minimum occurred for H_{clad} of 300 nm. This is attributed to the fact that, for smaller H_{clad} values, the I.L. increases due to the decreased overlap between the electric field intensity profiles of the photonic mode and the total coupled field at the front facet of the hybrid waveguide. For higher H_{clad} values L_c further increases, leading to higher I.L. as it was also reported in [34]. During simulations, the I.L. was determined after launching the quasi-TE mode of a 360×800 nm strip based Si_3N_4 waveguide and calculating the power that is coupled to the pure SPP mode.

That was realized by utilizing the built-in mode expansion monitors of *Lumerical Solutions* software to ensure that the forward propagating power is isolated and to calculate only the power that is
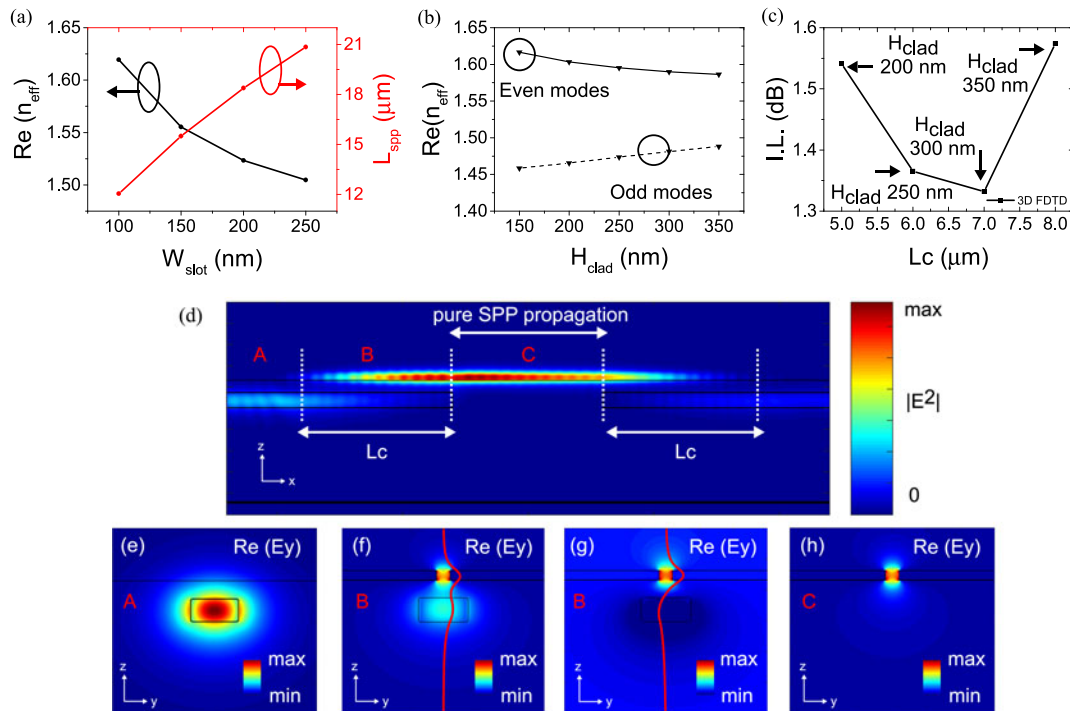
Fig. 2. (a) Effective refractive index (n_{eff}) and plasmonic propagation length (L_{spp}) for the SPP mode as function of W_{slot}. (b) Effective refractive index (n_{eff}) versus cladding thickness for the even and odd modes and (c) simulated I.L. as a function of L_c. (d) Electric field intensity ($|E^2|$) along the direction of propagation in the middle of the plasmo-photonic waveguide (y = 0) for L_c of 7 μm. (e)–(h) Electric field distribution Re(Ey) for photonic, even, odd and the pure SPP mode.

coupled into the pure SPP mode. This data was then normalized to the power of the photonic mode. For each investigated L_c value, the mode expansion monitor was settled 2 μm away from the end facet of the plasmonic waveguide and the calculated I.L. was normalized by subtracting the induced SPP damping incorporated after 2 μm of propagation. Fig. 2(d) illustrates the electric field intensity profile ($|E^2|$) along the direction of propagation and in the middle of the plasmo-photonic waveguide (y = 0). This graph shows how the photonic mode is converted to the pure SPP mode and back to the photonic mode by interrupting the photonic waveguides after an overlapping length equal to an L_c of 7 μm. Fig. 2(e)–(h) show the electric field distribution (Re(Ey)) for the photonic, even, odd and the pure SPP mode profile, respectively supported at the different stages of the structure. Finally, we investigated by means of numerical simulations (3 D FDTD) the tolerance of the plasmonic-to-photonic interface insertion loss for alignment errors of ±300 nm between the slot and the Si_3N_4 in the lateral direction [i.e., y-direction as it is denoted in Fig. 1(a)]. Numerical simulations have shown an increase of 1 dB for the plasmo-to-photonic interface insertion loss considering an alignment error of 300 nm. The refractive indices used in the simulations for the Si_3N_4, LTO, SiO_2 and water at 1.55 μm were 1.996,1.444,1.444 and 1.311-0.0001348i, respectively [35], [36]. During simulations we used the same refractive index value for both the LTO and the SiO_2 layers. The complex refractive indices used for gold and Ti at 1.55 μm were 0.26-11i and 4.04-3.82i, respectively [37], [36].

3. Fabrication and Measurement Results

The silicon nitride waveguides and grating couplers (GCs) were fabricated using standard 6" silicon wafers with 2.2 μm of thermally grown SiO_2 and optical projection lithography. The 360 nm thick
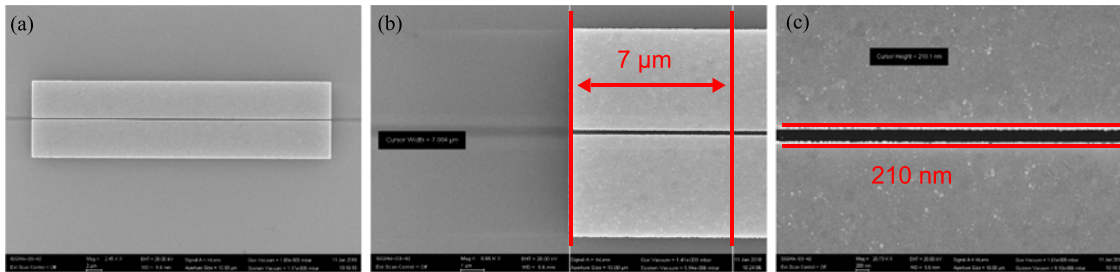
Fig. 3. SEM images. (a) Top-view of the plasmonic slot waveguide deposited on top of the Si_3N_4 waveguide. Close-up view for (b) the fabricated plasmonic waveguide with an L_c of 7 μm and (c) the plasmonic slot with a W_{slot} of 210 nm.
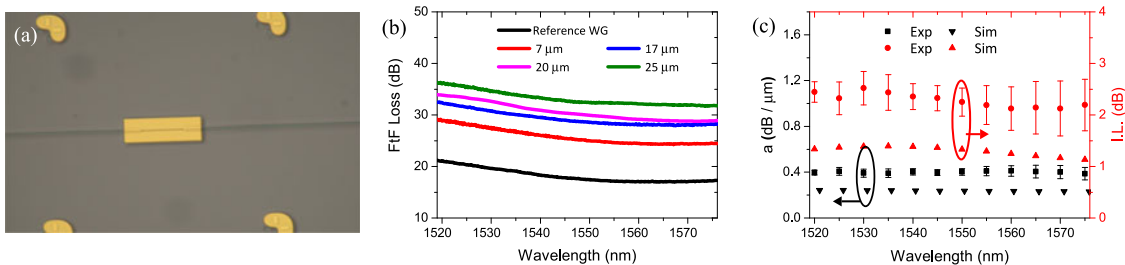

Fig. 4. (a) Microscope image depicting a plasmonic slot waveguide on top of an oxide cladded Si_3N_4 waveguide. (b) FtF loss budget for the measured test structures (c) Experimental and simulated I.L and plasmonic propagation loss as function of wavelength in water.

Si_3N_4 waveguide layer has been deposited in a low-pressure-chemical-vapor-deposition-process (LPCVD). Waveguide structures and markers have been defined by an i-line stepper tool. Reactive ion etching with CHF_3 and He chemistry was used for the structure transfer. Then 660 nm of SiO_2 (Low-temperature-oxide - LTO) was deposited by LPCVD for the cladding layer. To improve the SiO_2 quality and avoid additional losses, due to hygroscopic properties, the wafers have been annealed for several hours at 1000 °C. Planarization of the SiO_2 surface was done by spin coating spin-on-glass (SOG) and subsequent etching in CHF_3 plasma. The process cycle of SOG coating and dry etching was repeated twice, leaving only a level difference less than a few tens on nanometers above the LTO surface and away from silicon nitride waveguides. The plasmonic slot waveguides were deposited by a lift-off process using e-beam lithography, thermal evaporation of gold and lift-off. The e-beam lithography has been performed at 20 kV acceleration voltage on a ~220 nm thick Allresist CSAR62 resist coating. In this stage the alignment was based on the recognition of the markers that were previously patterned in the Si_3N_4 layer covered with LTO. Resist development took place in the AR600-546 developer, followed by rinsing in AR600-60. Before metal evaporation a descumming stage was also realized for 2 minutes in an oxygen-plasma cleaner. The target thickness for gold was 150 nm.

A very thin (3 nm) titanium layer has been deposited by e-gun evaporation prior to the gold layer for an improved adhesion of Au on the sample. The lift-off process has been realized in AR600-71 remover bath and the final rinsing in acetone and isopropanol. Scanning-Electron-Microscope (SEM) images for the fabricated structure are shown in Fig. 3.

Fig. 3(a) illustrates a top-view of the deposited plasmonic slot waveguide on top of the photonic waveguide, while Fig. 3(b) and (c) show a close-up view of the fabricated samples with a W_{slot} of 210 nm. Fig. 4(a) shows a microscope image of the fabricated plasmo-photonic waveguide. In order to measure the plasmonic propagation loss in water and the I.L. of the photonic-to-plasmonic interface, we fabricated test structures with different lengths (7, 17, 20 and 25 μm) of the pure plasmonic part of the waveguide and W_{slot} of 200 nm. Among the test structures we incorporated
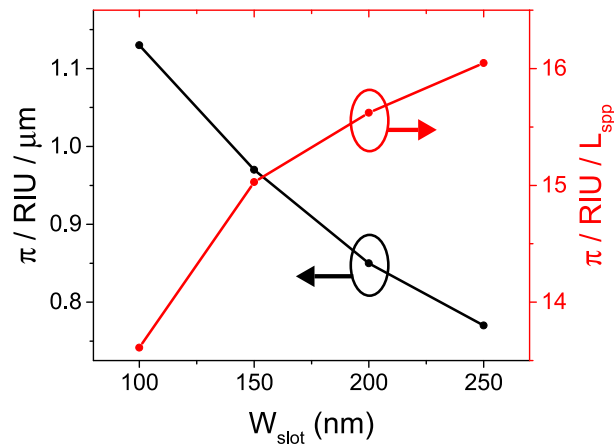
Fig. 5. Simulated accumulated phase change of the SPP mode over propagation distances of one micron (left-black) and one L_{spp} (right-red) as a function of W_{slot}.

a reference waveguide comprising of a 1 cm long straight Si_3N_4 waveguide. During optical characterization we carried out cut-back measurements by sweeping the wavelength of a tunable laser source from 1.52 μm to 1.575 μm. Fig. 4(b) presents results for the fiber-to-fiber (FtF) loss budget of the characterized test structures as a function of wavelength. The plasmonic propagation losses in water were calculated for wavelengths ranging from 1.52 μm to 1.575 μm with a step of 5 nm, performing least-squares linear fitting on the FtF loss budget data of the interface test structures with increasing slot length. Fig. 4(c) shows the plasmonic propagation loss in water as a function of wavelength, revealing 0.4 dB/μm losses at 1.55 μm, that correspond to an L_{spp} of 10.85 μm, closely following the theoretically predicted value of 0.24 dB/μm. The error bars correspond to the standard deviation deduced from the linear fitting process. To calculate the insertion loss of the photonic-to-plasmonic interface I.L. per single transition, the FtF losses of the reference Si_3N_4 waveguide structure were subtracted from the intercept values obtained by this linear fitting process and the resulting loss value was divided by a factor of two. The experimental I.L. that was derived from this calibration process is depicted in Fig. 4(c), showing a value of 2.24 $\pm$ 0.3 dB at 1.55 μm. Fig. 4(c) shows also the numerical results obtained from broadband simulations for a single vertical transition. Broadband simulations were performed taking into account the dispersive properties of gold, revealing interface losses of 1.35 dB at 1.55 μm, being in good agreement with experimentally obtained data.

4. Sensing Simulation

Following the good agreement between theory and experiment we investigate theoretically the sensitivity of the proposed plasmo-photonic waveguide to refractive index changes of the applied liquid cladding by calculating the accumulated phase change per refractive index unit (RIU) over a propagation distance equal to an L_{spp} length of 18.3 μm. This investigation estimates the potential benefits of this plasmo-photonic waveguide in biosensing applications if embedded in interferometric sensor layouts. A refractive index change ($\triangle n$) of 0.01 was introduced during simulations to the overlying water and the numerical results revealed a SPP mode with an effective index n_{eff} of 1.521 at 1.55 μm, increased by $\triangle n_{eff} = 0.006$ compared to its initial value with unperturbed aqueous solution. Using this $\triangle_{neff}$ value, the accumulated phase change over a length of L_{spp} is calculated to be 0.85 π for a $\triangle n = 10^{-2}$, which translates to 15.6 π/RIU/L_{spp} or, alternatively, to 0.85 π/RIU/μm. Fig. 5 presents the simulated phase change of the proposed plasmo-photonic waveguide accumulated over propagation distances equal to one micron or one L_{spp} for different W_{slot} values. Typical experimental results reported for photonic sensing waveguides hardly exceed

0.27 π/RIU/μm [38], using photonic slot configurations. In this context, the proposed waveguide solution presents a clear advantage towards realizing compact and highly sensitive sensors by tripling phase change accumulation per unit length when compared to photonic counterparts.

5. Conclusion

We have demonstrated, the design, fabrication and experimental characterization of water cladded Au-based plasmonic slot waveguides vertical coupled with interrupted Si$_3$N$_4$ waveguides at 1550 nm. Experimental measurements being in agreement with numerical simulations revealed a photonic-to-plasmonic I.L. of 2.24 $\pm$ 0.3 dB and an L$_{spp}$ of 10.8 μm at 1550 nm. Numerical simulations suggested also an accumulated phase change of 15.6 π/RIU/L$_{spp}$ or 0.85 π/RIU/μm in the pure plasmonic waveguide clearly highlighting the promise of the proposed waveguide when used as the optical transducer in compact and highly sensitive interferometric biosensors.

References

[1] S. Papaioannou *et al.*, "A 320 Gb/s-throughput capable 2 $\times$ 2 silicon-plasmonic router architecture for optical interconnects," *J. Lightw. Technol.*, vol. 29, no. 21, pp. 3185–3195, Dec. 2011.

[2] D. Kalavrouziotis *et al.*, "0.48 Tb/s (12 $\times$ 40 Gb/s) WDM transmission and high-quality thermo-optic switching in dielectric loaded plasmonics," *Opt. Exp.*, vol. 20, pp. 7655–7662, 2012.

[3] S. Papaioannou *et al.*, "Active plasmonics in WDM traffic switching applications," *Sci. Rep.*, vol. 2, 2012, Art. no. 652.

[4] C. Hoessbacher *et al.*, "Plasmonic modulator with >170 GHz bandwidth demonstrated at 100 GBd NRZ," *Opt. Exp.*, vol. 25, no. 3, pp. 1762–1768, 2017.

[5] J. Gosciniak, V. S. Volkov, S. I. Bozhevolnyi, L. Markey, S. Massenot, and A. Dereux, "Fiber-coupled dielectric-loaded plasmonic waveguides," *Opt. Exp.*, vol. 18, no. 5, pp. 5314–5319, 2010.

[6] J. Gosciniak *et al.*, "Thermo-optic control of dielectric-loaded plasmonic waveguide components," *Opt. Exp.*, vol. 18, no. 2, pp. 1207–1216, 2010.

[7] N. Pleros *et al.*, "Tb/s switching fabrics for optical interconnects using hetero integration of plasmonics and silicon photonics: The FP7 PLATON approach," in *Proc. 23rd Annu. Meet. IEEE Photon. Soc.*, Denver, CO, USA, 2010, pp. 165–166.

[8] X. Sun, D. Dai, L. Thylén, and L. Wosinski, "High-sensitivity liquid refractive-index sensor based on a Mach–Zehnder interferometer with a double-slot hybrid plasmonic waveguide," *Opt. Exp.*, vol. 23, no. 20, pp. 25689–25699, 2015.

[9] G. D. Osowiecki, E. Barakat, A. Naqavi, and H. P. Herzig, "Vertically coupled plasmonic slot waveguide cavity for localized biosensing applications," *Opt. Exp.*, vol. 22, pp. 20871–20880, 2014.

[10] C. Delacour *et al.*, "Efficient directional coupling between silicon and copper plasmonic nanoslot waveguides: Toward metal-oxide-silicon nanophotonics," *Nano Lett.*, vol. 10, pp. 2922–2926, 2010.

[11] O. Tsilipakos *et al.*, "Interfacing dielectric-loaded plasmonic and silicon photonic waveguides: Theoretical analysis and experimental demonstration," *IEEE J. Quantum Electron.*, vol. 48, no. 5, pp. 678–687, May 2012.

[12] A. Melikyan, M. Kohl, M. Sommer, C. Koos, W. Freude, and J. Leuthold, "Photonic-to-plasmonic mode converter," *Opt. Lett.*, vol. 39, no. 12, pp. 3488–3491, 2014.

[13] C. T. Chen, X. Xu, A. Hosseini, Z. Pan, and R. T. Chen, "High efficiency silicon strip waveguide to plasmonic slot waveguide mode converter," *Proc. SPIE*, vol. 9368, 2015, Art. no. 936809.

[14] R. M. Briggs, J. Grandidier, S. P. Burgos, E. Feigenbaum, and H. A. Atwater, "Efficient coupling between dielectric-loaded plasmonic and silicon photonic waveguides," *Nano Lett.*, vol. 10, no. 12, pp. 4851–4857, 2010.

[15] S. Zhu, G. Lo, and D. Kwong, "Silicon nitride based plasmonic components for CMOS back-end-of-line integration," *Opt. Exp.*, vol. 21, no. 20, pp. 23376–23390, 2013.

[16] R. Wan, F. Liu, X. Tang, Y. Huang, and J. Peng, "Vertical coupling between short range surface plasmon polariton mode and dielectric waveguide mode," *Appl. Phys. Lett.*, vol. 94, no. 14, 2009, Art. no. 41104.

[17] F. Liu *et al.*, "Extremely high efficient coupling between long range surface plasmon polariton and dielectric waveguide mode," *Appl. Phys. Lett.*, vol. 95, no. 9, 2009, Art. no. 091104.

[18] M. P. Nielsen *et al.*, "Adiabatic nanofocusing in hybrid gap plasmon waveguides on the silicon-on-insulator platform," *Nano Lett.*, vol. 16, no. 2, pp. 1410–1414, 2016.

[19] C. Xiang and J. Wang, "Long-range hybrid plasmonic slot waveguide," *IEEE Photon. J.*, vol. 5, no. 2, Apr. 2013, Art. no. 4800311.

[20] B. L. Mohamed, A. Swillam, and A. S. Helmy, "Hybrid orthogonal junctions: Wideband plasmonic slot-silicon waveguide couplers," *Opt. Exp.*, vol. 18, pp. 27048–27059, 2010.

[21] R. Yang, R. A. Wahsheh, Z. Lu, and M. A. G. Abushagur, "Efficient light coupling between dielectric slot waveguide and plasmonic slot waveguide," *Opt. Lett.*, vol. 35, pp. 649–651, 2010.

[22] L. Chen, J. Shakya, and M. Lipson, "Subwavelength confinement in an integrated metal slot waveguide on silicon," *Opt. Lett.*, vol. 31, pp. 2133–2135, 2006.

[23] D. Ketzaki, G. Dabos, J. C. Weeber, A. Dereux, D. Tsiokos, and N. Pleros, "A directional coupling scheme for efficient coupling between Si$_3$N$_4$ photonic and hybrid slot-based plasmonic waveguide," *Proc. SPIE*, vol. 10106, 2017, Art. no. 1010615.

[24] M. Ono *et al.*, "Deep-subwavelength plasmonic mode converter with large size reduction for Si-wire waveguide," *Optica*, vol. 3, pp. 999–1005, 2016.

[25] B. Q. Zhu and H. K. Tsang, "High coupling efficiency silicon waveguide to metal–insulator–metal waveguide mode converter," *J. Lightw. Technol.*, vol. 34, no. 10, pp. 2467–2472, May 2016.

[26] R. A. Wahsheh and M. A. G. Abushagur, "Experimental and theoretical investigations of an air-slot coupler between dielectric and plasmonic waveguides," *Opt. Exp.*, vol. 24, pp. 8237–8242, 2016.

[27] L. Chen, X. Li, and D. Gao, "An efficient directional coupling from dielectric waveguide to hybrid long-range plasmonic waveguide on a silicon platform," *Appl. Phys. B*, vol. 111, no. 1, pp. 15–19, 2013.

[28] J. Tian, S. Yu, W. Yan, and M. Qiu, "Broadband high-efficiency surface-plasmon-polariton coupler with silicon-metal interface," *Appl. Phys. Lett.*, vol. 95, 2009, Art. no. 013504.

[29] Y. Ming, Z. J. Wu, H. Wu, F. Xu, and Y. Q. Lu, "Surface plasmon interferometer based on wedge metal waveguide and its sensing applications," *IEEE Photon. J.*, vol. 4, no. 1, pp. 291–299, Feb. 2012.

[30] Y. Ming *et al.*, "Squeezing a surface plasmon through quadratic nonlinear interactions," *ACS Photon.*, vol. 3, no. 11, pp. 2074–2082, 2016.

[31] C. Lee, F. Dieleman, J. Lee, C. Rockstuhl, S. A. Maier, and M. Tame, "Quantum plasmonic sensing: Beyond the shot-noise and diffraction limit," *ACS Photon.*, vol. 3, no. 6, pp. 992–999, 2016.

[32] Lumerical Solutions, Inc., [Online]. Available: http://www.lumerical.com/tcad-products/mode/

[33] Lumerical Solutions, Inc., [Online]. Available: http://www.lumerical.com/tcad-products/fdtd/

[34] Q. Li and M. Qiu, "Structurally-tolerant vertical directional coupling between metal-insulator-metal plasmonic waveguide and silicon dielectric waveguide," *Opt. Exp.*, vol. 18, no. 15, pp. 15531–15543, 2010.

[35] K. Luke, Y. Okawachi, M. R. E. Lamont, A. L. Gaeta, and M. Lipson, "Broadband mid-infrared frequency comb generation in a Si_3N_4 microresonator," *Opt. Lett.*, vol. 40, no. 21, pp. 4823–4826, 2015.

[36] E. D. Palik, *Handbook of Optical Constants of Solids I–III*. New York, NY, USA: Academic, 1998.

[37] J.-C. Weeber *et al.*, "Characterization of CMOS metal based dielectric loaded surface plasmon waveguides at telecom wavelengths," *Opt. Exp.*, vol. 25, no. 1, pp. 394–408, 2017.

[38] A. F. Gavela, D. G. García, J. C. Ramirez, and L. M. Lechuga, "Last advances in silicon-based optical biosensors," *Sensors*, vol. 16, no. 3, 2016, Art. no. 285.